THE JOURNAL OF PHYSICAL CHEMISTRY C
A JOURNAL OF THE AMERICAN CHEMICAL SOCIETY

pubs.acs.org/JPCC

Article

Electrocatalytic Reduction of CO_2 to CO over Ag(110) and Cu(211) Modeled by Grand-Canonical Density Functional Theory

Yousef A. Alsunni, Abdulaziz W. Alherz, and Charles B. Musgrave*

Cite This: *J. Phys. Chem. C* 2021, 125, 23773–23783

Read Online

ACCESS | Metrics & More | Article Recommendations | Supporting Information

ABSTRACT: We report the results of modeling CO_2 reduction (CO_2R) to CO over Ag(110) and Cu(211) surfaces at different applied potentials using grand-canonical density functional theory (GC-DFT), a method specifically designed to accurately model electrochemical systems. In addition to demonstrating GC-DFT's ability to accurately model electrochemical processes, we also compare it with the computational hydrogen electrode (CHE) approach. GC-DFT predicts that the geometries of these reacting systems strongly depend on the applied potential, and the Helmholtz free energies vary nonlinearly with the applied potential, which contradicts a central assumption of the CHE approach. The CHE approach neglects the change in the number of electrons on the electrode surface at different applied potentials, which reduces its accuracy as the potential changes from the potential of zero charge. Our results further demonstrate that the grand free energies of the reaction intermediates not only depend on the value of the applied potential but also on the metal surface type, adsorption site, and adsorbate. GC-DFT's ability to predict the effect of the applied potential on adsorbate geometry enables it to evaluate different possible reaction mechanisms at different applied potentials. For instance, GC-DFT predicts that the first step of CO_2R likely switches from proton-coupled electron transfer to sequential electron transfer and then proton transfer at more reducing potentials, a result that cannot be determined by the CHE because it assumes that all electron transfers are coupled to proton transfers and neglects the effect of the applied potential on the adsorbate geometry.

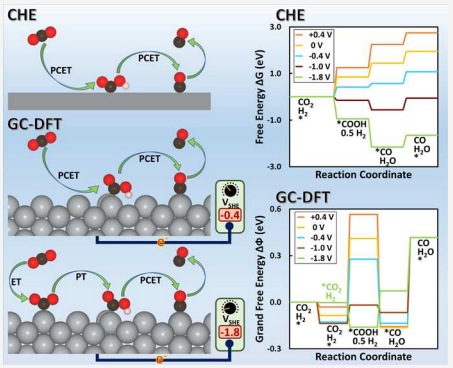

INTRODUCTION

As the cost to generate electric power from solar and wind continues its steep decline, carbon-free electrochemical processes that exploit inexpensive electricity will become increasingly economically viable. Electrocatalysis to produce various value-added products is one area that is poised to exploit this disruptive opportunity. However, although these processes will be driven by renewably produced energy, their viability still requires that they utilize this energy efficiently, for instance, by minimizing overpotentials. Consequently, discovering efficient electrocatalysts and electrocatalytic processes is central to accelerating the development of a carbon-free electrochemical industry. Quantum chemical modeling is a powerful approach to developing new catalysts and chemical processes because it provides a fundamental description of atomistic systems and can accurately predict their properties ab initio. While this promise is being fulfilled for a variety of areas, its application to electrocatalysis encounters many obstacles. This is primarily a result of the computational complexity of realistically describing the electrified electrocatalyst interface to properly evaluate the effects of the applied potential and the electrolyte. These challenges have motivated various approaches that either neglect these effects completely or simplify them to make the quantum mechanical problem computationally tractable.

Most computational studies that have modeled electrochemical reactions have employed density functional theory (DFT) to describe the electronic structure of the catalyst and reacting species, either vacuum or continuum models of the electrolyte to model solvent effects and either neglect the applied bias entirely or employ the computational hydrogen electrode (CHE) approach[1] to approximate the effects of the applied potential on the energetics of the reaction mechanism.[2−10] The CHE model's appeal stems from its simplicity in estimating the free energy as a function of potential for reactions involving proton-coupled electron transfer (PCET) steps with simple algebraic corrections to DFT-computed electronic energies. The central idea of the CHE framework is to express hydrogen gas in equilibrium with a solvated proton and an electron at the Fermi level of a Pt electrode of the standard hydrogen electrode (SHE) at 0 V, as described by the following equation

Received: August 23, 2021
Revised: October 7, 2021
Published: October 21, 2021

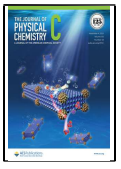

$$\frac{1}{2}H_{2(g)} \leftrightarrow H_{(aq)}^{+} + e^{-} \quad (1)$$

Therefore, the chemical potential of the solvated proton−electron pair ($\mu(H^+) + \mu(e^-)$) is related to that of gaseous hydrogen $\mu(H_{2(g)})$ as a function of the applied potential φ through the equation

$$\mu(H^+) + \mu(e^-) = 0.5\mu(H_{2(g)}) - e\varphi \quad (2)$$

where e is the elementary positive charge. This reference is incorporated into the energies of PCET steps to simply shift their DFT-predicted energies by the electrode potential φ times e.

The CHE approach utilizes conventional DFT and thus assumes a constant number of electrons to model the charged electrode surface regardless of the applied potential. Therefore, the electronic structure of the catalyst and reacting species is that of the neutral system, and the proton−electron pair in the PCET step is directly transferred to the adsorbate. Additionally, the DFT-computed energies of reaction intermediates do not correspond to a constant applied potential because the potential of zero charge (PZC) depends sensitively on the adsorbate identity, adsorption site, and binding mode. Hence, while the CHE approach assumes that every reaction step occurs at a Fermi level aligned with the applied potential, in practice, it is based on DFT energies computed at a constant number of electrons and Fermi levels that vary as the reaction progresses. Furthermore, the CHE assumes that the catalyst and adsorbate geometries at all biases are fixed at the atomic positions predicted by DFT for the system with a fixed number of electrons. Therefore, the CHE model neglects the deviation from integer charge states of the electrode surface. It also assumes that the linear correction to the DFT energy that accounts for the electrochemical energy of electron transfer (ET) is independent of the catalyst surface and the adsorption site. This simplification could lead to considerable error because the electronic structures of each surface and reactive site are unique, and consequently, the localization of the additional electron density on the surface at more reducing potentials distributes itself to these sites differently at each potential. In addition to the errors associated with these approximations, the CHE was found to not estimate accurate adsorption energies in the presence of electrolyte coadsorption.[11] These possible sources of error must be evaluated to determine whether the CHE is sufficiently accurate to reliably guide the discovery and development of electrocatalysts. If not, a more sophisticated computational method is needed to provide an accurate and fundamental tool to rationally design and computationally prototype candidate electrocatalysts and their associated processes.

Grand-canonical DFT (GC-DFT) provides a fundamentally correct description of electrified interfaces and a correct model of electrocatalysis when coupled with a sufficiently detailed solvent model of the solvent and electrolyte. GC-DFT calculates the grand free energy at an arbitrary potential by optimizing the grand free energy while self-consistently solving for the number of electrons that matches the applied potential rather than calculating the electronic energy of the system with a fixed number of electrons. The grand free energy is defined as $\Phi = A - \mu N$, where A, μ, and N are the Helmholtz free energy, chemical potential, and total number of electrons, respectively. GC-DFT enables accurate calculation of the electronic energy and adsorbate geometry and should thus provide a reliable prediction of the energetics of electrochemical reaction pathways. Furthermore, it enables the comparison of various possible reaction mechanisms at different applied potentials. In this work, we applied GC-DFT to theoretically analyze the electrochemical CO_2 reduction (CO_2R) reaction on two well-studied CO_2R catalysts and compared these results to those computed using the CHE.

Electrocatalytic CO_2R has been under intense study due to its potential to be the key part of a closed-loop solution that meets growing energy demands while achieving net-zero carbon emissions by recycling CO_2 into value-added fuels. Achieving efficient and selective CO_2R into valuable products is extraordinarily challenging. One common approach to CO_2R is to first convert CO_2 into fuel precursors, such as syngas (CO + H_2), followed by Fischer−Tropsch synthesis to produce hydrocarbons.[12−15] While syngas production is typically performed as a thermochemical process, several promising electrochemical systems with high selectivity toward syngas have been recently discovered.[16] Electrochemical production of CO from CO_2 is particularly attractive because Faradaic efficiencies above 95% can be achieved,[17−21] although it requires the use of expensive catalysts such as Au or Ag, which makes its industrial-scale implementation economically challenging. For an electrocatalytic CO_2R process to be economically viable at a sufficiently large scale to make a significant impact on atmospheric CO_2 concentrations and to produce chemicals on a scale that could displace petrochemical production, the catalyst must be stable, selective, and composed of earth-abundant metals. Previous studies of CO_2R have demonstrated that several transition metal catalysts, such as Au, Ag, Zn, Pd, and Ga, are highly selective toward CO.[22−28] Copper was found to readily catalyze CO_2R to CO but with low selectivity as it promotes C−C coupling reactions and yields a variety of compounds and thus requires subsequent separation processes that lower its overall efficiency and raise its cost.[29] Despite the identification of various potential reaction mechanisms and the publication of numerous experimental and computational studies of CO_2R, debate about these reaction pathways, and their energetics and activity, continues unabated. The nature of the influence of the applied field on the mechanism and its associated energetics is even less well-understood, although it lies at the very heart of the electrochemical process. Even for electrocatalysts that, in contrast to Cu, are highly selective, determining and understanding the detailed electrocatalytic mechanism remain an unsolved problem.

Obtaining a clear, detailed, and fundamental understanding of the microscopic reaction mechanism is crucial to optimizing CO_2R and increasing the yield of specific products. Unfortunately, the obstacles to ab initio modeling of electrocatalytic processes described above have hindered theory from elucidating the underlying principles that govern these processes, while the limitations of the CHE approach may provide misleading descriptions of CO_2R and other electrochemical processes. Consequently, fundamentally correct and detailed descriptions of electrocatalysis remain elusive even for what are expected to be simple processes, such as CO_2R to CO on d-block metals. Again, the primary reason for this is the challenge of quantum mechanical modeling of the electrochemical interface, for example, by DFT, which involves both the complexities of describing the solvation of the reacting interface by the electrolyte and the influence of the applied bias. To avoid these difficulties, most computational

https://doi.org/10.1021/acs.jpcc.1c07484
J. Phys. Chem. C 2021, 125, 23773−23783

models of electrocatalysis have used DFT to model the reacting electrocatalyst surface in vacuum[30−33] and in the absence of an applied potential. In this work, we employ GC-DFT as implemented within the JDFTx code to model the solvated and electrified electrocatalyst interface where the number of electrons is determined self-consistently to align the Fermi level with the applied potential.[34] We have chosen to model the mechanism of CO_2R to CO catalyzed by two well-studied systems, Ag(110) and Cu(211), to compare how the GC-DFT and CHE methods differ in describing the electrochemical reaction energetics.

COMPUTATIONAL METHODS

Computational Details. To model CO_2R on the Ag(110) surface, slabs of 32 Ag atoms in four layers were periodically repeated using a supercell with approximate dimensions of 6 × 8 × 30 Å, which included >15 Å of vertical space between the surface atoms and the bottom of the periodic image of the slab. This unit cell was tested to produce similar energies to larger cells and was sampled using a 5 × 4 × 1 Γ-point centered *k*-point grid. For the *COOH adsorbate on the Ag surface, a 6 × 16 × 30 Å supercell containing 64 Ag atoms was utilized with a 5 × 2 × 1 *k*-point grid. The doubling of the unit cell size in the direction parallel to the adsorbate was done to eliminate hydrogen bonding between *COOH and its periodic image. To model CO_2R on the Cu(211) surface, 72 Cu atoms in four layers to form a Cu(211) slab were periodically repeated using a supercell of approximately 13 × 8 × 22 Å with >15 Å of separation between the top of the slab and the bottom of its periodic image with a 2 × 3 × 1 *k*-point grid. The Monkhorst−Pack algorithm was utilized to select the k-point mesh for all slabs.[35]

GC-DFT calculations were performed using the joint DFT (JDFTx) code,[34] the PBE-D2 exchange−correlation functional, SG15 pseudopotentials, and a plane-wave basis with a 20 Hartree cutoff energy. Fermi−Dirac smearing with a 0.001 Hartree width was used to accelerate the self-consistent field convergence. Electronic structure calculations were converged when total energy differences of $<10^{-8}$ Hartree were attained, while geometry optimizations were converged when total energy differences of $<10^{-6}$ Hartree were attained.[36] The charge-asymmetry corrected, local-response, and nonlocal-cavity (CANDLE) solvation model was employed to treat solvation effects on charged/adsorbed species.[36] Conventional DFT was employed to obtain CHE pathways using the same computational settings described above and the same solvent model, CANDLE. The GC-DFT method describes the effect of the applied bias on the reaction by self-consistently minimizing the grand free energy by solving for the number of electrons that results in a Fermi level, that is, the chemical potential of electrons μ, that matches the applied potential. Applied biases ranging from −1.8 to +0.4 V for Ag and from −1.3 to +0.6 V for Cu versus SHE were explored.

Reference Electrode of the CHE versus GC-DFT. Here, we describe what is implicitly defined as the 0 V potential according to the CHE and GC-DFT formalisms. GC-DFT sets a specific chemical potential corresponding to 0 V versus SHE that was benchmarked by Sundararaman et al. against experiments for the CANDLE solvent model interfaced with DFT descriptions of the electronic structure of various catalyst surfaces.[36−38] On the other hand, the CHE references the potential for the DFT-computed energies. This is a fundamental limitation of the CHE approach because conventional DFT minimizes the geometries to the lowest possible electronic energy—not the grand free energy—with the number of electrons fixed to that of the neutral, unbiased system; that is, the potential floats to the PZC. Thus, the CHE assigns the reference potential to the PZC. From the more fundamental grand-canonical perspective, the CHE computes geometries and energies of intermediates at different, unaligned potentials because the PZC of any specific electrode surface depends on the adsorbate. We refer to these types of calculations as "unbiased". Consequently, the CHE computes reaction pathways that represent a sequence of electrochemical reaction steps that occur at a variable potential rather than a constant potential consistent with the experiment. In this study, we reference the CHE potential to the PZC of the clean surface slab.

Energy Calculations and Reaction Coordinate Diagrams. Using the CHE approach, the free energy of a reaction intermediate formed by *n* PCET steps is calculated as a function of the applied potential φ as

$$\Delta G(\varphi) = \Delta G_{\text{Corr DFT}} + ne\varphi \tag{3}$$

where *n* is the number of electron−proton pairs transferred to the adsorbed intermediate and $\Delta G_{\text{Corr DFT}}$ is the DFT-computed energy of the PCET step corrected for the zero-point energy (ZPE) and *S*, although in practice these corrections are rarely implemented. Thus, the CHE linearly shifts the corrected DFT-computed energy by $ne\varphi$ for the system under an applied potential φ. In the CHE equation (eq 3), the inclusion of the ZPE and S only improves the accuracy of the constant term $\Delta G_{\text{Corr DFT}}$ and is not affected by φ. For this reason, and because they do not contribute significantly to differences between the CHE and GC-DFT-calculated reaction energetics under various φ and the computational expense of the phonon calculations required to compute these contributions, this work omits these terms in the CHE calculation.

The similarity between the form of the CHE equation and the definition of the grand free energy entice some researchers to interpret the CHE free energy as an approximation to the grand free energy $\Delta\Phi = \Delta A - \Delta\mu\Delta N$.[38] The electrode potential φ is equivalent up to an offset to μ and the term $\Delta G_{\text{Corr DFT}}$ approximates the change in Helmholtz free energy ΔA. Thus, by setting ΔN equal to $-ne$, eq 3 is obtained. This is a debatable interpretation of the CHE model equation because it implies that the CHE equation makes several assumptions not stated in the original CHE paper,[1] such as ΔA being constant at different values of φ and that the total number of electrons in the system is reduced by one for each PCET step. In fact, the total number of electrons changes nonlinearly with the applied potential, not because of the PCET reaction. The original description of the CHE approach does not claim that its calculated energy represents the grand free energy but that it corrects the DFT-calculated free energy to account for the applied potential.[1,2,39] Therefore, in this study, we interpret the CHE approach as it was originally defined.

The GC-DFT method computes the number of electrons of the grand-canonical ensemble at constant μ, *V*, and *T* with the chemical potential of electrons μ consistent with an arbitrary applied potential. Therefore, GC-DFT accurately calculates the change in the reaction grand free energy caused by the applied bias to the degree that the underlying DFT exchange−correlation functional correctly describes the *N*-electron system. In addition, GC-DFT enables computation of accurate adsorbate geometries at each applied potential to avoid the

https://doi.org/10.1021/acs.jpcc.1c07484
J. Phys. Chem. C 2021, 125, 23773−23783

common assumption that the geometry remains constant in the unbiased structure. This is a powerful ability because it enables the determination of whether an electrochemical reaction follows the PCET mechanism or the stepwise (ET-PT) mechanism from the computed geometry of adsorbed CO_2 at different applied potentials.

The energies of reaction coordinate diagrams are plotted relative to the energies of reference species. In the case of CO_2R, it is convenient to choose $CO_2 + H_2 + *$, where * represents the solvated bare metal surface, at infinite separation as the thermodynamic reference so that its grand free energy at each applied potential is subtracted from that of all other reaction intermediates and the final products to calculate their energies. Equations 4−8 were used to calculate the grand free energies of formation of each species relative to the reference state

$$\Phi_{CO_2} + \Phi_* + \Phi_{H_2} = 0(\text{reference}) \tag{4}$$

$$\Delta\Phi_{*CO_2} = \Phi_{*CO_2} + \Phi_{H_2} - (\Phi_{CO_2} + \Phi_* + \Phi_{H_2}) \tag{5}$$

$$\Delta\Phi_{*COOH} = \Phi_{*COOH} + 0.5\Phi_{H_2} - (\Phi_{CO_2} + \Phi_* + \Phi_{H_2}) \tag{6}$$

$$\Delta\Phi_{*CO} = \Phi_{*CO} + \Phi_{H_2O} - (\Phi_{CO_2} + \Phi_* + \Phi_{H_2}) \tag{7}$$

$$\Delta\Phi_{CO+*} = \Phi_{CO} + \Phi_* + \Phi_{H_2O} - (\Phi_{CO_2} + \Phi_* + \Phi_{H_2}) \tag{8}$$

Equation 5 is used to calculate the grand free energy of CO_2 adsorption or the energy required to bring CO_2 up to the surface (also denoted as $\Delta\Phi_{*CO2}$, although CO_2 is not favorably bound to the surface) for cases where CO_2 chemisorption is unfavorable. Equations 6 and 7 are used to calculate the grand free energies of formation of *COOH and *CO + H_2O, respectively, from the reference species, and eq 8 represents the grand free energy of the overall reaction.

The CHE approach assumes that the free energies to form *COOH and *CO, which both involve PCET, are their DFT-predicted energies shifted by $ne\varphi$. To apply the CHE approach, we used eq 3 for the PCET steps (*CO_2 and *COOH protonation) so that the free energies of formation of *COOH and *CO are written as a function of the applied potential φ and the corrected unbiased DFT energies $G_i|_{\text{Corr DFT}}$

$$\Delta G_{*COOH}(\varphi) = G_{*COOH}|_{\text{Corr DFT}} + 0.5G_{H_2}|_{\text{Corr DFT}} - (G_{CO_2}|_{\text{Corr DFT}} + G_* |_{\text{Corr DFT}} + G_{H_2}|_{\text{Corr DFT}}) + e\varphi \tag{9}$$

$$\Delta G_{*CO}(\varphi) = G_{*CO}|_{\text{Corr DFT}} + G_{H_2O}|_{\text{Corr DFT}} - (G_{CO_2}|_{\text{Corr DFT}} + G_* |_{\text{Corr DFT}} + G_{H_2}|_{\text{Corr DFT}}) + 2e\varphi \tag{10}$$

Previous studies that used the CHE approach varied the overall reaction free energy with the applied potential.[1,2,39] For instance, because $CO_{(aq)}$ is produced from $CO_{2(aq)}$ with two PCET steps, the CHE shifts the free energy of formation of $CO_{(aq)}$ and hence the overall reaction free energy by $2e\varphi$. This implicitly assumes that the desorption energy of CO is independent of the applied potential because the free energies of formation of *CO and $CO_{(g)}$ are shifted by the same amount, $2e\varphi$. The CO desorption step is written as

$$*CO \rightarrow CO_{(aq)} + * \tag{11}$$

and the CO desorption grand free energy ($\Delta\Phi_{des}$) is computed by the equation

$$\Delta\Phi_{des} = \Phi_{CO_{(aq)}} + \Phi_* - \Phi_{*CO} = \Delta A_{des} - \mu\Delta N_{des} \tag{12}$$

Because the adsorption of CO perturbs the electronic structure of the bare metal surface, the number of electrons required to maintain a specific Fermi energy of both the clean surface and the surface with adsorbed CO differs. Consequently, the term $-\mu\Delta N_{des}$ in eq 12 is nonzero and so, $\Delta\Phi_{des}$ is a function of φ. This differs from the CHE in which the desorption free energy is independent of φ. Herein, we implemented the CHE as it was intended and compare its predicted reaction coordinate diagrams to those computed with GC-DFT. As such, we calculate the free energy of formation of the $CO_{(aq)}$ product within the CHE using eq 13

$$\Delta G_{CO}(\varphi) = G_{CO}|_{\text{Corr DFT}} + G_*|_{\text{Corr DFT}} + G_{H_2O}|_{\text{Corr DFT}} - (G_{CO_2}|_{\text{Corr DFT}} + G_* |_{\text{Corr DFT}} + G_{H_2}|_{\text{Corr DFT}}) + 2e\varphi \tag{13}$$

RESULTS AND DISCUSSION

Reaction Mechanism. The CO_2R to CO reaction mechanism has been proposed to be composed of three elementary steps, as described by eqs 14−16.

$$CO_{2(aq)} + * + H_{(aq)}^+ + e^- \leftrightarrow *COOH \tag{14}$$

$$*COOH + H_{(aq)}^+ + e^- \leftrightarrow *CO + H_2O_{(l)} \tag{15}$$

$$*CO \leftrightarrow CO_{(aq)} + * \tag{16}$$

The first step is a PCET from the electrode to $CO_{2(aq)}$ to form *COOH adsorbed on the Ag cathode surface. In contrast, at highly reducing (negative) potentials, the Ag surface is experimentally observed to facilitate stepwise, sequential ET and proton transfer (PT) steps to first form $*COO^-$, which is then protonated to yield the *COOH intermediate, as described by eqs 17 and 18.[12,40]

$$CO_{2(aq)} + * + e^- \leftrightarrow *COO^- \tag{17}$$

$$*COO^- + H^+ \leftrightarrow *COOH \tag{18}$$

Catalysts that decouple the ET and PT steps may provide flexibility for designing surfaces and reaction conditions that take advantage of this feature.[12] After *COOH is formed by either pathway, it undergoes another PCET to form $H_2O_{(l)}$ and *CO. The final step of the proposed mechanism is the desorption of *CO from the electrode surface. To optimize the binding of the first intermediate, which is correlated to the activation of CO_2, it is essential to know the reaction energy diagram and whether the first intermediate is *COOH or $*COO^-$. Furthermore, the applied potential φ likely significantly affects the energies of these reduced species. Therefore, it is crucial to study the effect of φ on the reaction diagram because it likely influences the reaction mechanism and could direct it to follow either a PCET or an ETPT pathway for the first elementary step.

Previous theoretical studies that used DFT corrected by the CHE approximation have found that among the elementary reaction steps, the formation of *CO via the *COOH

https://doi.org/10.1021/acs.jpcc.1c07484
J. Phys. Chem. C 2021, 125, 23773−23783

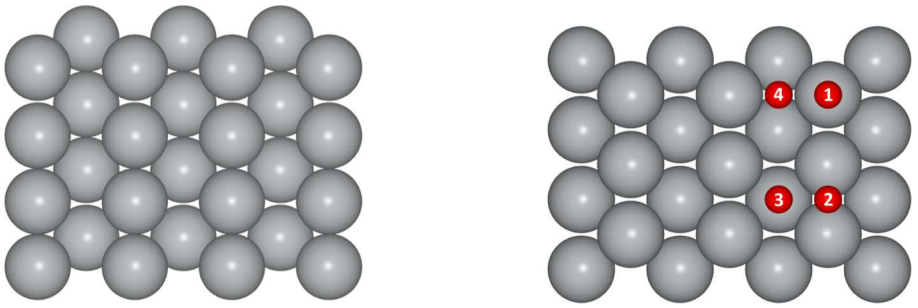

Figure 1. Side view (left) and top view (right) of the Ag (110) surface with possible adsorption sites marked in red. Site 1 is a ridge atop site, Site 2 a ridge bridge site, Site 3 a trough atop site, and Site 4 a trough bridge site. This work computes the CO_2R reaction pathway at Site 1, which is the most favorable adsorption energy site.

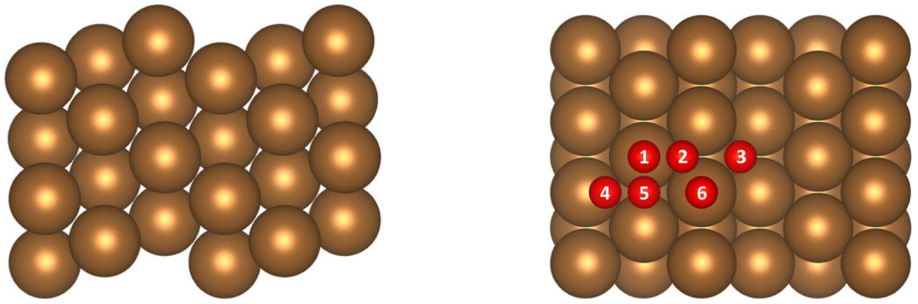

Figure 2. Side view (left) and top view (right) of the Cu(211) surface with possible adsorption sites marked in red. This work computes the CO_2R reaction pathway on Sites 1 and 6, which are the two most favorable adsorption energy sites. Site 1 is a terrace atop site and Site 6 a step atop site.

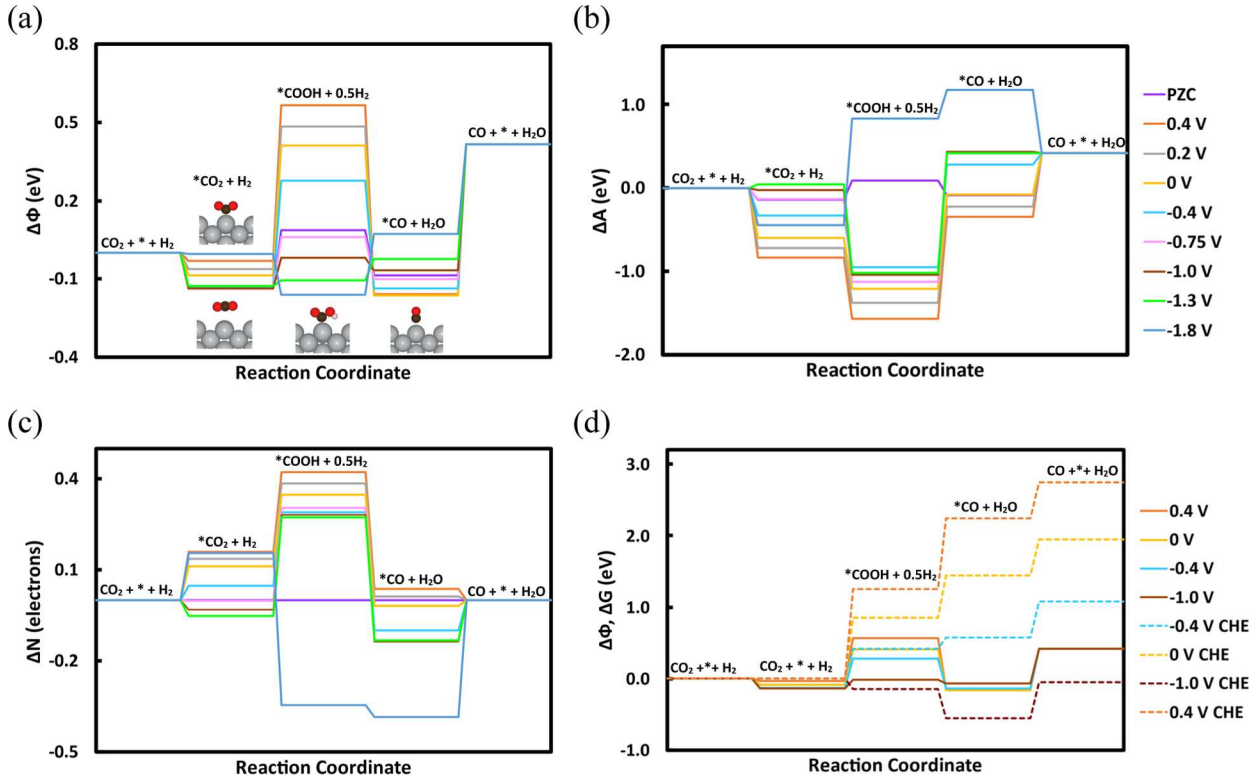

Figure 3. (a) CO_2R reaction coordinate diagram of GC-DFT-computed intermediate energies on Ag(110). *COOH formation is more sensitive to bias than other intermediates due to its more pronounced effect on the PZC and its susceptibility to relax to different geometries at different applied potentials. (b) Reaction coordinate diagram of intermediates' Helmholtz free energies. ΔA depends nonlinearly on bias, invalidating the CHE linear approximation. (c) Reaction coordinate diagram for the change in the number of electrons N of the surface. $\Delta N > 0$ indicates that extra electrons are added to the system. (d) Comparison of intermediate energies calculated by the GC-DFT (Φ) and CHE (G) approaches.

intermediate (eq 15) requires the lowest overpotential on the Ag catalyst. These studies also indicate that adsorption of CO_2 to the surface either by a PCET step to form *COOH or by a single ET step to form $*COO^-$ is the rate-limiting step.[41,42]

https://doi.org/10.1021/acs.jpcc.1c07484
J. Phys. Chem. C 2021, 125, 23773−23783

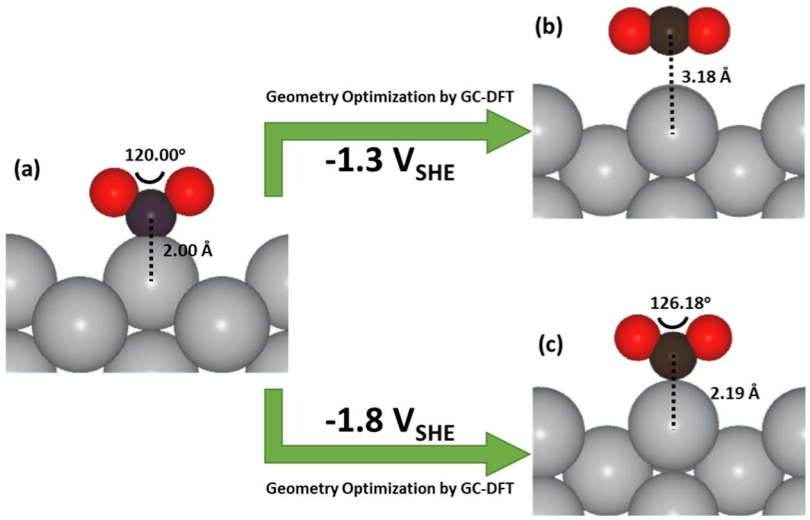

Figure 4. Effect of applied potential on CO_2 adsorption on Ag. (a) Initial geometry used for the GC-DFT geometry optimizations for each potential. (b) At −1.3 V_{SHE}, GC-DFT geometry optimization predicts that CO_2 is physisorbed in a linear configuration at a Ag−C distance of 3.18 Å. (c) At −1.8 V_{SHE}, GC-DFT predicts that CO_2 chemisorbs as an unprotonated anion in a bent $*CO_2^-$ configuration via a 2.19 Å Ag−C bond.

Other experimental studies have demonstrated that reaction conditions, such as electrolyte concentration,[43] the local pH,[44] or the catalyst structure, such as the presence of grain boundaries on the catalyst surface,[21,23,45] can be manipulated to improve the binding of CO_2 and/or reaction intermediates to the catalyst surface.

Facets and Adsorption Sites. Identification of the active sites on the reactive surface of the catalyst is the first step in predicting the reaction coordinate diagram. At thermodynamic equilibrium, low energy surfaces are more prevalent among the facets of the catalyst nanoparticle. To determine the equilibrium shape of the crystalline nanoparticle, that is, the relative area of its various facets, the computed surface energies are used within the Wulff Construction[46] to minimize the nanoparticle energy of the catalyst of interest. Previous studies used the Wulff construction to determine that Ag nanoparticles consist of six facets.[47] The lowest energy surface, and hence the largest area equilibrium facet, is the (111) crystal plane. In contrast, the highest energy surface is the (110) crystal plane. Although the (110) facet has a higher surface energy and therefore does not make up a significant fraction of the crystal faces present on the Ag nanoparticle, it has been identified in a previous study as the most active surface for CO_2R to CO. Other low energy facets were found to also catalyze the reduction of CO_2 to CO but with higher reaction intermediate energies and barriers.[12]

The Ag (110) surface contains four unique adsorption sites, as illustrated in Figure 1. Our calculations predict that the atop site (Site 1) is the most favorable adsorption site for all intermediates of the CO_2R reaction. We found that the *COOH intermediate on the bridge site (Site 2) is less favorable than that at Site 1 and that it does not adsorb at the second-layer bridge and atop positions (Sites 3 and 4). Hence, we computed the reaction pathway for CO_2R activated at Site 1.

The Cu (211) surface, displayed in Figure 2, has been identified as the most active surface for CO_2R.[3,48] This study considers reactions on the two sites with the most favorable adsorption energies: the atop site of step atoms (Site 6, Figure 2) and the atop site of terrace atoms neighboring a step (Site 1, Figure 2), respectively.

CO_2R Reaction Coordinate Diagram on the Ag(110) Surface. We first computed the reaction coordinate diagrams of the CO_2R reaction catalyzed by Ag(110) at multiple biases directly using GC-DFT and indirectly using the CHE approach as described above. Figure 3a shows the effect of the applied bias on the reaction coordinate diagram on Ag(110) as calculated by GC-DFT. The reaction starts with aqueous CO_2, $H_{2(g)}$, and a bare Ag surface at infinite separation, which we use as the reference state for this reaction. The first intermediate along the reaction coordinate is CO_2 physisorbed or chemisorbed onto the Ag(110) surface. Although a few previous studies have applied grand-canonical approaches to study the energetics of electrochemical reactions, they did not consider the effect of the applied potential on the reactant geometry.[49−51] On the other hand, this work shows that at all biases considered except −1.8 V_{SHE}, GC-DFT predicts that CO_2 does not adsorb because geometry optimizations of CO_2 in a bent geometry placed near the surface to bind through its C atom converge to a linear structure that drifts away from the surface. However, among the applied potentials considered in this study, GC-DFT predicts that at −1.8 V_{SHE}, $*CO_2$ adsorbs as an unprotonated anion, Figure 4. This indicates that the threshold potential for CO_2 adsorption is between −1.3 V_{SHE} and −1.8 V_{SHE}. At more reducing potentials than the threshold potential, CO_2 adsorbs on Ag, which may indicate that the reaction follows an ET-PT CO_2 adsorption mechanism.[12] The reaction coordinate diagram illustrated in Figure 3a indicates that the physisorbed CO_2 is followed by a higher energy *COOH intermediate, suggesting that the first PCET step is likely rate-limiting. However, at −1.8 V_{SHE}, protonation of $*COO^-$ is exergonic.

We next calculated the formation energy of the *COOH intermediate at various applied potentials using eq 6. GC-DFT predicts that more negative biases further stabilize *COOH, as indicated by the lower computed values of $\Delta\Phi_{*COOH}$ at the more reducing potentials shown in Figure 3a. This occurs because the more negatively charged surface at more reducing potentials donates more electron density—which is higher in energy at the higher Fermi levels of these more negative applied biases—through π-backbonding to the π^* states (*C═O) of CO_2, which lowers the energy to form *COOH

https://doi.org/10.1021/acs.jpcc.1c07484
J. Phys. Chem. C 2021, 125, 23773−23783

by PCET or PT to $*COO^-$, respectively. The energy of *COOH is more sensitive to the applied potential. This contradicts the CHE approach, which predicts that the energy of *CO is more sensitive to the applied potential than *COOH because *CO is produced by two PCET steps. Next, PCET to *COOH releases a H_2O from the adsorbed intermediate to yield *CO, which desorbs into the aqueous phase to produce $CO_{(aq)}$. The grand free energies plotted in Figure 3a show that more reducing values of φ slightly increase the formation energy of *CO and hence reduce its desorption energy. Thus, more reducing biases enhance the reduction of CO_2 to CO by promoting the formation of *COOH and desorption of CO.

Equation 8 computes the overall grand free energy of the reaction

$$CO_{2(aq)} + H_{2(aq)} \leftrightarrow CO_{(aq)} + H_2O_{(aq)} \quad (19)$$

The overall grand free energy of the reaction at constant electron chemical potential μ could be decomposed as

$$\Delta\Phi_{rxn} = \Delta A_{rxn} - \mu\Delta N_{rxn} \quad (20)$$

Because the overall reaction does not change the total number of electrons ($\Delta N_{rxn} = 0$) and all reactant and product species are in solution at infinite separation, the applied bias has no effect on the reaction Helmholtz free energy, ΔA_{rxn}, or the reaction grand free energy, $\Delta\Phi_{rxn}$. Therefore, the difference between the reactant and product states that grand free energies are independent of the applied bias and so is the overall reaction grand free energy, as shown by the GC-DFT-computed grand free energies plotted in Figure 3a.

As described by eq 3, the CHE linearly relates the applied potential to the free energy. As mentioned above, ΔA is sufficient to quantify the DFT free energy, which is calculated within the canonical ensemble (N, V, T). Since ΔA is strongly affected by the number of electrons and the CHE ignores the noninteger charge state of the electrode surface, this could lead to large errors in the CHE-predicted free energy. Figure 3b plots the GC-DFT-computed ΔA along the CO_2R reaction coordinate as a function of bias and shows that ΔA depends nonlinearly on φ. This is caused by surface charging where the number of electrons on the catalyst surface increases in a nonlinear manner as φ becomes more reducing, which leads to additional electronic repulsion, population of states, and renormalization of the density of states, especially near the Fermi level. These effects influence the geometries of the intermediates, which in turn affect the electronic structure. This shows that to the degree φ affects these properties, the hypothesis of a linear relation between φ and the free energy of the reactions involving PCET steps is invalid. Moreover, Figure 5 plots the Helmholtz free energies of the PCET steps to form *COOH and *CO, denoted as ΔA_{*COOH} and ΔA_{*CO}, respectively. The plot shows that the applied potential has a nonlinear effect on the Helmholtz free energies of the PCET steps, which contradicts the primary assumption of the CHE approach.

GC-DFT computes the electronic structure of the electrified interface by self-consistently adjusting the number of electrons in the system such that the electron chemical potential (i.e., the Fermi level) of the optimized N-electron wavefunction/density is equal to φ. Figure 3c plots the change in the number of electrons of the surface for each step along the reaction coordinate. The number of electrons ΔN_{Step} transferred to or from the reservoir to maintain the Fermi level of the system at

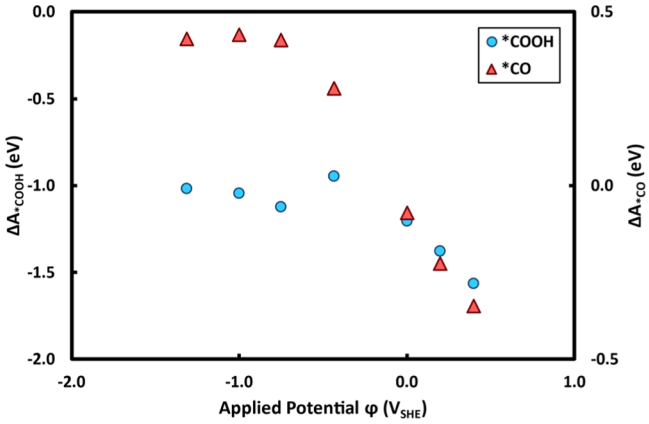

Figure 5. Effect of the applied potential on the energies of the PCET steps to form *COOH and *CO. Both plots exhibit a range of potentials over which the effects of the applied potential on ΔA_{*COOH} and ΔA_{*CO} are nonlinear.

the specified applied bias varies with each adsorbate because each adsorbate interacts differently with the electrode and thus uniquely perturbs the electronic structure of the clean surface and shifts the PZC differently. For instance, *COOH increases the PZC of the bare Ag surface by 0.23 V, while *CO decreases the PZC of the Ag clean surface by 0.18 V.

To compare the reaction thermodynamics predicted by GC-DFT and the CHE, we plotted the formation energies of the intermediates and products as a function of φ in Figure 3d. GC-DFT describes the reaction pathway by the grand free energy, while the CHE employs the Gibbs free energy. The reaction pathway computed at -1.8 V_{SHE} cannot be obtained by the CHE approach because it proceeds via a stepwise ET-PT mechanism for which the CHE approach is not applicable. The differences between the CHE- and GC-DFT-predicted energies at different applied potentials are relatively large for *COOH and are especially large for *CO and $CO_{(aq)}$. Furthermore, the difference in the reaction pathways computed by the two methods increases with larger values of $|\varphi|$ and the number of the PCET steps because the larger integer n multiplied by the applied potential φ in eq 3 causes larger shifts in the CHE free energy. At -1.0 V_{SHE}, the CHE predicts that forming the *COOH intermediate is exergonic, while GC-DFT predicts that forming *COOH is endergonic. This results because GC-DFT computes a lower energy for physisorbed $*CO_2$, while the CHE cannot be applied to calculate the energy of $*CO_2$. GC-DFT predicts that *CO formation is downhill except at more reducing potentials that stabilize *COOH more than *CO. However, the CHE predicts the opposite trend that *COOH is more stable than *CO, but at high reducing potentials, the *COOH to *CO step is exergonic. Figure 3d also shows that the CHE predicts that the overall reaction free energy could be manipulated by adjusting φ, while GC-DFT predicts that the overall reaction grand free energy is insensitive to φ. This difference arises because the CHE calculates the free energy of formation of $CO_{(aq)}$ referenced to reducing $CO_{2(aq)}$ with two PCET steps that together shift the DFT-predicted energy by $2e\varphi$. Conceptually, this results in the implicit assumption by the CHE that the two electrons that reduce CO_2 are transferred to CO_2 directly through the solution and not the metal cathode. In contrast, GC-DFT correctly treats the electrons as being transferred from the external reservoir through the metal

https://doi.org/10.1021/acs.jpcc.1c07484
J. Phys. Chem. C 2021, 125, 23773−23783

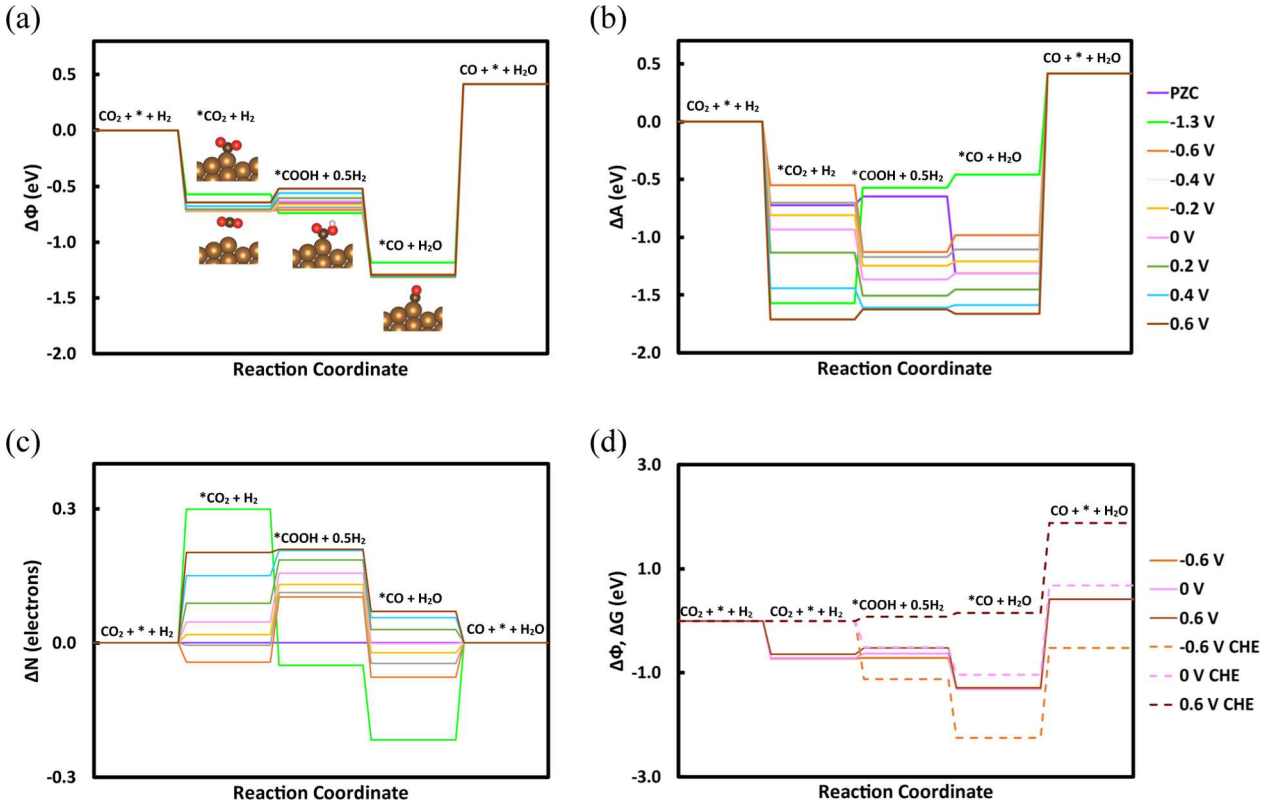

Figure 6. (a) CO_2R reaction coordinate diagram of GC-DFT-computed intermediate energies on the atop step site of Cu(211). *COOH formation is more sensitive to bias than other intermediates due to its more pronounced effect on the PZC and its susceptibility to relax to different geometries at different applied potentials. (b) Reaction coordinate diagram of the intermediates' Helmholtz free energies. ΔA is nonlinearly sensitive to bias, invalidating the CHE linear approximation. (c) Reaction coordinate diagram for the change in the number of electrons N along the reaction coordinate. $\Delta N > 0$ indicates that electrons are added to the system. (d) Comparison between the reaction coordinate diagrams predicted by the GC-DFT (Φ) and CHE (G) approaches.

electrode. Thus, GC-DFT calculates a constant overall grand free energy of reaction at all applied potentials because N is not changed by the overall chemical reaction; consequently, the term $\mu\Delta N_{rxn}$ in eq 20 is zero for the GC-DFT grand free energy of the overall reaction.

CO_2R Reaction Coordinate Diagram on the Cu(211) Surface. The CHE approach assumes that the shift in intermediate energies caused by the applied potential is independent of the electrode material, crystal facet, and adsorption site. To examine the validity of this assumption, we also studied CO_2R catalyzed by Cu and specifically computed the effect of the applied potential on the CO_2R reaction energetics at the two most stable adsorption sites of Cu(211): the atop site on steps (Site 6, Figure 2) and the atop sites on terrace atoms neighboring steps (Site 1, Figure 2). The elementary reaction steps for CO_2R on Cu are similar to those on Ag. The reaction coordinate diagram for CO_2R at the step site of Cu(211) plotted in Figure 6a shows that CO_2 physisorption is favorable, as was predicted by GC-DFT for CO_2 adsorption on Ag(110). At −1.3 V_{SHE}, GC-DFT-optimized geometries show that CO_2 chemisorbs to Cu and is slightly less stable than its physisorbed linear state at less reducing potentials. As on Ag(110), formation of *COOH from chemisorbed *CO_2 is exergonic, while formation of *COOH from physisorbed *CO_2 is endergonic. Figure 6a also shows that *COOH is somewhat stabilized as φ becomes more reducing, while more reducing potentials have little effect on *CO stability. Figure 6a shows that the desorption of *CO from the Cu surface is unfavorable and insensitive to φ. Thus, our results predict long lifetimes for *CO on Cu at all potentials, indicating susceptibility to further reduction on Cu, as observed experimentally.[3,52−56] Figure 6b shows that ΔA for all intermediates on this site is nonlinear and highly sensitive to φ. This results because the step site is less sterically hindered, which allows adsorbed intermediates to relax to a wider range of structures, which influences the electronic structure at different values of φ and enables intermediates to attain lower grand free energies that can decrease even further with φ. Figure 6c shows how N changes for each intermediate at the various applied potentials considered. A different N is required for each intermediate at each specified potential. The change in N follows a similar trend at all potentials considered except at −1.3 V_{SHE} because at this φ, the reaction follows the ET-PT stepwise mechanism in which N increases more as CO_2 adsorbs during the ET step to form *COO^- and then decreases during the subsequent PT step that forms *COOH. Figure 6d shows that GC-DFT predicts that the grand free energy of *COOH is less sensitive to φ than is its free energy predicted by the CHE, which exaggerates the sensitivity of *COOH to applied bias. The difference between both approaches is even more striking for the energies of the *CO intermediate.

Unlike at Site 6, the GC-DFT-computed grand free energies of intermediates (see Figure S1a) adsorbed at Site 1 (atop terrace atoms) predict that at −1.3 V_{SHE}, the reaction proceeds through PCET instead of by ET-PT. In addition, this terrace

https://doi.org/10.1021/acs.jpcc.1c07484
J. Phys. Chem. C 2021, 125, 23773−23783

site is more sterically hindered and thus provides less spatial freedom for *COOH to relax to different geometries relative to the step site, resulting in a higher endergonic *COOH formation energy. By examining Figure S1b,c, we deduced the strong correlation between A and N, especially when no significant changes in the geometry are predicted. At −1.3 V_{SHE}, ΔA and ΔN for $*CO_2$ formation follow the same trend with φ because CO_2 is not adsorbed and there is no significant change in its geometry.

As expected, the CHE predicts a stronger effect of φ on the reaction coordinate diagram (see Figure S1d). We found that GC-DFT predicts that the first PCET step to form *COOH is always endergonic but that the CHE predicts it to be exergonic for reducing potentials. In contrast, GC-DFT predicts that the second PCET step to form *CO is always exergonic, while the CHE predicts it to be endergonic at oxidizing potentials of ∼0.5 V_{SHE}.

The GC-DFT-computed reaction coordinate diagrams for CO_2R on Ag(110) and Cu(211) show that φ has a more pronounced effect on CO_2R reaction energies on Ag(110) than those on Cu(211). In addition, the effect of φ on adsorbates differs between the step and terrace sites of the Cu(211) surface considered. Such effects are not predicted by the CHE approach, which does not calculate the grand free energy and assumes equivalent energy shifts for the applied potential regardless of the electrode surface and adsorption site.

CONCLUSION

In this study, we utilized the GC-DFT method and CHE approach to generate reaction coordinate diagrams for CO_2R to CO over the Ag(110) and Cu(211) surfaces at different applied potentials. GC-DFT predicts that intermediate geometries are affected by the applied potential, and the free energies of the reacting system are nonlinearly affected by varying the applied potential, which contradict a central assumption of the CHE approach. The CHE overestimates the effect of the applied potential on the energetics of the electrochemical reaction because it ignores the noninteger charge state of the biased electrode surface. In addition, the CHE computes a qualitatively incorrect energy for electrochemical processes driven by an external bias, which are open systems in which electrons are exchanged with a reservoir. The grand free energy computed by GC-DFT is the appropriate free energy to describe such systems.

GC-DFT predicts that the effect of the applied potential on the grand free energy depends on the metal surface type and adsorption site. The ability of GC-DFT to optimize geometries at different applied potentials enables it to predict the effect of the applied potential on the reaction coordinate and thus to evaluate various possible reaction mechanisms on the catalyst surface. Of the two mechanisms that have been proposed in the literature for the first elementary step of CO_2R to CO over metal surfaces, PCET and the sequential ET then PT, GC-DFT shows that CO_2R to CO on Ag(110) and Cu(211) likely proceeds via PCET at mildly reducing potentials and via sequential ET and then PT at highly reducing potentials, a result that cannot be predicted by the CHE approach given its assumption that all ETs occur by PCET at fixed intermediate geometries at all applied potentials.

ASSOCIATED CONTENT

Supporting Information

The Supporting Information is available free of charge at https://pubs.acs.org/doi/10.1021/acs.jpcc.1c07484.

Results for the CO_2R reaction on the terrace atop site of Cu(211), reaction coordinate diagram of GC-DFT-computed intermediate energies, reaction coordinate diagram of intermediates' Helmholtz free energies, reaction coordinate diagram for the change in the number of electrons along the reaction coordinate, and comparison of intermediate energies calculated by the GC-DFT and CHE approaches (PDF)

AUTHOR INFORMATION

Corresponding Author

Charles B. Musgrave − *Department of Chemical and Biological Engineering, Renewable and Sustainable Energy Institute, and Materials Science and Engineering Program, University of Colorado Boulder, Boulder, Colorado 80309, United States;* orcid.org/0000-0002-5732-3180; Email: charles.musgrave@colorado.edu

Authors

Yousef A. Alsunni − *Chemical Engineering Department, King Fahd University of Petroleum and Minerals, Dhahran 31261, Saudi Arabia; Department of Chemical and Biological Engineering, University of Colorado Boulder, Boulder, Colorado 80309, United States;* orcid.org/0000-0002-2417-8482

Abdulaziz W. Alherz − *Department of Chemical and Biological Engineering, University of Colorado Boulder, Boulder, Colorado 80309, United States;* orcid.org/0000-0001-7529-3483

Complete contact information is available at: https://pubs.acs.org/10.1021/acs.jpcc.1c07484

Notes

The authors declare no competing financial interest.

ACKNOWLEDGMENTS

We gratefully acknowledge use of the Summit supercomputer, which is supported by the University of Colorado Boulder. We also thank King Fahd University of Petroleum and Minerals and Kuwait University for financial support. C.B.M. gratefully acknowledges support from the National Science Foundation (CBET-2016225) and support by the U.S. Department of Energy, Office of Science, Basic Energy Sciences, under award #DE-SC0022247. This work utilized the supercomputing resources from the University of Colorado Boulder Research Computing Group, which is supported by the National Science Foundation [awards ACI-1532235 and ACI-1532236], the University of Colorado Boulder, and Colorado State University.

REFERENCES

(1) Nørskov, J. K.; Rossmeisl, J.; Logadottir, A.; Lindqvist, L.; Kitchin, J. R.; Bligaard, T.; Jonsson, H. Origin of the Overpotential for Oxygen Reduction at a Fuel-Cell Cathode. *J. Phys. Chem. B* **2004**, *108*, 17886−17892.

(2) Hansen, H. A.; Varley, J. B.; Peterson, A. A.; Nørskov, J. K. Understanding Trends in the Electrocatalytic Activity of Metals and

Enzymes for CO_2 Reduction to CO. *J. Phys. Chem. Lett.* **2013**, *4*, 388−392.
(3) Durand, W. J.; Peterson, A. A.; Studt, F.; Abild-Pedersen, F.; Nørskov, J. K. Structure Effects on the Energetics of the Electrochemical Reduction of CO_2 by Copper Surfaces. *Surf. Sci.* **2011**, *605*, 1354−1359.
(4) Peterson, A. A.; Abild-Pedersen, F.; Studt, F.; Rossmeisl, J.; Nørskov, J. K. How Copper Catalyzes the Electroreduction of Carbon Dioxide into Hydrocarbon Fuels. *Energy Environ. Sci.* **2010**, *3*, 1311−1315.
(5) Guo, L.; Guo, S. Mechanistic Understanding of CO_2 Reduction Reaction Towards C_1 Products by Molecular Transition Metal Porphyrin Catalysts. *Int. J. Hydrogen Energy* **2021**, *46*, 10608.
(6) Gono, P.; Pasquarello, A. High-Performance Niooh/Feooh Electrode for Oer Catalysis. *J. Chem. Phys.* **2021**, *154*, 024706.
(7) Zhang, Y.; Fang, L.; Cao, Z. Atomically Dispersed Cu and Fe on N-Doped Carbon Materials for CO_2 Electroreduction: Insight into the Curvature Effect on Activity and Selectivity. *RSC Adv.* **2020**, *10*, 43075−43084.
(8) Chan, K. A Few Basic Concepts in Electrochemical Carbon Dioxide Reduction. *Nat. Commun.* **2020**, *11*, 1−4.
(9) Alfonso, D. R. CO_2 Conversion on Ligand-Protected Au25 Nanoparticle: The Role of Structural Inhomogeneity in the Promotion of the Electrocatalytic Process. *Phys. Status Solidi B* **2020**, *258*, 2000387.
(10) Rendón-Calle, A.; Builes, S.; Calle-Vallejo, F. A Brief Review of the Computational Modeling of CO_2 Electroreduction on Cu Electrodes. *Curr. Opin. Electrochem.* **2018**, *9*, 158−165.
(11) Alfonso, D.; Tafen, D.; Kauffmann, D. First-Principles Modeling in Heterogeneous Electrocatalysis. *Catalysts* **2018**, *8*, 424.
(12) Firet, N. J.; Smith, W. A. Probing the Reaction Mechanism of CO_2 Electroreduction over Ag Films Via Operando Infrared Spectroscopy. *ACS Catal.* **2017**, *7*, 606−612.
(13) Martín, A. J.; Larrazábal, G. O.; Pérez-Ramírez, J. Towards Sustainable Fuels and Chemicals through the Electrochemical Reduction of CO_2: Lessons from Water Electrolysis. *Green Chem.* **2015**, *17*, 5114−5130.
(14) Dahl, S.; Chorkendorff, I. Towards Practical Implementation. *Nat. Mater.* **2012**, *11*, 100−101.
(15) Jiao, F.; Li, J.; Pan, X.; Xiao, J.; Li, H.; Ma, H.; Wei, M.; Pan, Y.; Zhou, Z.; Li, M.; Miao, S.; Li, J.; Zhu, Y.; Xiao, D.; He, T.; Yang, J.; Qi, F.; Fu, Q.; Bao, X. Selective Conversion of Syngas to Light Olefins. *Science* **2016**, *351*, 1065−1068.
(16) Pardal, T.; Messias, S.; Sousa, M.; Machado, A. S. R.; Rangel, C. M.; Nunes, D.; Pinto, J. V.; Martins, R.; da Ponte, M. N. Syngas Production by Electrochemical CO_2 Reduction in an Ionic Liquid Based-Electrolyte. *J. CO2 Util.* **2017**, *18*, 62−72.
(17) Rosen, B. A.; Salehi-Khojin, A.; Thorson, M. R.; Zhu, W.; Whipple, D. T.; Kenis, P. J. A.; Masel, R. I. Dt Whipple, Pja Kenis and Ri Masel. *Science* **2011**, *334*, 643−644.
(18) Larrazábal, G. O.; Martín, A. J.; Pérez-Ramírez, J. Building Blocks for High Performance in Electrocatalytic CO_2 Reduction: Materials, Optimization Strategies, and Device Engineering. *J. Phys. Chem. Lett.* **2017**, *8*, 3933−3944.
(19) Kumar, B.; Asadi, M.; Pisasale, D.; Sinha-Ray, S.; Rosen, B. A.; Haasch, R.; Abiade, J.; Yarin, A. L.; Salehi-Khojin, A. Renewable and Metal-Free Carbon Nanofibre Catalysts for Carbon Dioxide Reduction. *Nat. Commun.* **2013**, *4*, 1−8.
(20) Saberi Safaei, T.; Mepham, A.; Zheng, X.; Pang, Y.; Dinh, C.-T.; Liu, M.; Sinton, D.; Kelley, S. O.; Sargent, E. H. High-Density Nanosharp Microstructures Enable Efficient CO_2 Electroreduction. *Nano Lett.* **2016**, *16*, 7224−7228.
(21) Chen, Y.; Li, C. W.; Kanan, M. W. Aqueous CO_2 Reduction at Very Low Overpotential on Oxide-Derived Au Nanoparticles. *J. Am. Chem. Soc.* **2012**, *134*, 19969−19972.
(22) Hatsukade, T.; Kuhl, K. P.; Cave, E. R.; Abram, D. N.; Jaramillo, T. F. Insights into the Electrocatalytic Reduction of CO_2 on Metallic Silver Surfaces. *Phys. Chem. Chem. Phys.* **2014**, *16*, 13814−13819.
(23) Rosen, J.; Hutchings, G. S.; Lu, Q.; Rivera, S.; Zhou, Y.; Vlachos, D. G.; Jiao, F. Mechanistic Insights into the Electrorchemical Reduction of CO_2 to CO on Nanostructured Ag Surfaces. *ACS Catal.* **2015**, *5*, 4293−4299.
(24) Hara, K.; Sakata, T. Large Current Density CO_2 Reduction under High Pressure Using Gas Diffusion Electrodes. *Bull. Chem. Soc. Jpn.* **1997**, *70*, 571−576.
(25) Kim, C.; Jeon, H. S.; Eom, T.; Jee, M. S.; Kim, H.; Friend, C. M.; Min, B. K.; Hwang, Y. J. Achieving Selective and Efficient Electrocatalytic Activity for CO_2 Reduction Using Immobilized Silver Nanoparticles. *J. Am. Chem. Soc.* **2015**, *137*, 13844−13850.
(26) Noda, H.; Ikeda, S.; Oda, Y.; Imai, K.; Maeda, M.; Ito, K. Electrochemical Reduction of Carbon Dioxide at Various Metal Electrodes in Aqueous Potassium Hydrogen Carbonate Solution. *Bull. Chem. Soc. Jpn.* **1990**, *63*, 2459−2462.
(27) Hoshi, N.; Kato, M.; Hori, Y. Electrochemical Reduction of CO_2 on Single Crystal Electrodes of Silver Ag (111), Ag (100) and Ag (110). *J. Electroanal. Chem.* **1997**, *440*, 283−286.
(28) Hori, Y. i. Electrochemical CO_2 Reduction on Metal Electrodes. *Modern Aspects of Electrochemistry*; Springer, 2008; pp 89−189.
(29) Kuhl, K. P.; Cave, E. R.; Abram, D. N.; Jaramillo, T. F. New Insights into the Electrochemical Reduction of Carbon Dioxide on Metallic Copper Surfaces. *Energy Environ. Sci.* **2012**, *5*, 7050−7059.
(30) Yang, D.-R.; Liu, L.; Zhang, Q.; Shi, Y.; Zhou, Y.; Liu, C.; Wang, F.-B.; Xia, X.-H. Importance of Au Nanostructures in CO_2 Electrochemical Reduction Reaction. *Sci. Bull.* **2020**, *65*, 796−802.
(31) Sakong, S.; Groß, A. The Importance of the Electrochemical Environment in the Electro-Oxidation of Methanol on Pt (111). *ACS Catal.* **2016**, *6*, 5575−5586.
(32) Gossenberger, F.; Roman, T.; Groß, A. Hydrogen and Halide Co-Adsorption on Pt (111) in an Electrochemical Environment: A Computational Perspective. *Electrochim. Acta* **2016**, *216*, 152−159.
(33) Lv, X.; Wei, W.; Wang, H.; Huang, B.; Dai, Y. Multifunctional Electrocatalyst Ptm with Low Pt Loading and High Activity Towards Hydrogen and Oxygen Electrode Reactions: A Computational Study. *Appl. Catal., B* **2019**, *255*, 117743.
(34) Sundararaman, R.; Letchworth-Weaver, K.; Schwarz, K. A.; Gunceler, D.; Ozhabes, Y.; Arias, T. A. Jdftx: Software for Joint Density-Functional Theory. *SoftwareX* **2017**, *6*, 278−284.
(35) Ong, S. P.; Richards, W. D.; Jain, A.; Hautier, G.; Kocher, M.; Cholia, S.; Gunter, D.; Chevrier, V. L.; Persson, K. A.; Ceder, G. Python Materials Genomics (Pymatgen): A Robust, Open-Source Python Library for Materials Analysis. *Comput. Mater. Sci.* **2013**, *68*, 314−319.
(36) Sundararaman, R.; Goddard, W. A., III The Charge-Asymmetric Nonlocally Determined Local-Electric (Candle) Solvation Model. *J. Chem. Phys.* **2015**, *142*, 064107.
(37) Sundararaman, R.; Schwarz, K. Evaluating Continuum Solvation Models for the Electrode-Electrolyte Interface: Challenges and Strategies for Improvement. *J. Chem. Phys.* **2017**, *146*, 084111.
(38) Schwarz, K.; Sundararaman, R. The Electrochemical Interface in First-Principles Calculations. *Surf. Sci. Rep.* **2020**, *75*, 100492.
(39) Liu, X.; Xiao, J.; Peng, H.; Hong, X.; Chan, K.; Nørskov, J. K. Understanding Trends in Electrochemical Carbon Dioxide Reduction Rates. *Nat. Commun.* **2017**, *8*, 1−7.
(40) Kortlever, R.; Shen, J.; Schouten, K. J. P.; Calle-Vallejo, F.; Koper, M. T. M. Catalysts and Reaction Pathways for the Electrochemical Reduction of Carbon Dioxide. *J. Phys. Chem. Lett.* **2015**, *6*, 4073−4082.
(41) Peterson, A. A.; Nørskov, J. K. Activity Descriptors for CO_2 Electroreduction to Methane on Transition-Metal Catalysts. *J. Phys. Chem. Lett.* **2012**, *3*, 251−258.
(42) Shi, C.; Hansen, H. A.; Lausche, A. C.; Nørskov, J. K. Trends in Electrochemical CO_2 Reduction Activity for Open and Close-Packed Metal Surfaces. *Phys. Chem. Chem. Phys.* **2014**, *16*, 4720−4727.
(43) Kas, R.; Kortlever, R.; Yılmaz, H.; Koper, M. T. M.; Mul, G. Manipulating the Hydrocarbon Selectivity of Copper Nanoparticles in

https://doi.org/10.1021/acs.jpcc.1c07484
J. Phys. Chem. C 2021, 125, 23773−23783

CO_2 Electroreduction by Process Conditions. *ChemElectroChem* **2015**, *2*, 354−358.
(44) Ma, M.; Djanashvili, K.; Smith, W. A. Controllable Hydrocarbon Formation from the Electrochemical Reduction of CO_2 over Cu Nanowire Arrays. *Angew. Chem., Int. Ed.* **2016**, *55*, 6680−6684.
(45) Lee, H.-E.; Yang, K. D.; Yoon, S. M.; Ahn, H.-Y.; Lee, Y. Y.; Chang, H.; Jeong, D. H.; Lee, Y.-S.; Kim, M. Y.; Nam, K. T. Concave Rhombic Dodecahedral Au Nanocatalyst with Multiple High-Index Facets for CO_2 Reduction. *ACS Nano* **2015**, *9*, 8384−8393.
(46) Wulff, G. Xxv. Zur Frage Der Geschwindigkeit Des Wachsthums Und Der Auflösung Der Krystallflächen. *Z. für Kristallogr. - Cryst. Mater.* **1901**, *34*, 449−530.
(47) Tran, R.; Xu, Z.; Radhakrishnan, B.; Winston, D.; Sun, W.; Persson, K. 653 Sp Ong. Surface energies of elemental crystals. *Sci. Data* **2016**, *3*, 1−13.
(48) Kim, T.; Palmore, G. T. R. A Scalable Method for Preparing Cu Electrocatalysts That Convert CO_2 into C_{2+} Products. *Nat. Commun.* **2020**, *11*, 1−11.
(49) Huang, Y.; Nielsen, R. J.; Goddard, W. A., III Reaction Mechanism for the Hydrogen Evolution Reaction on the Basal Plane Sulfur Vacancy Site of MoS_2 Using Grand Canonical Potential Kinetics. *J. Am. Chem. Soc.* **2018**, *140*, 16773−16782.
(50) Liu, C.; Qian, J.; Ye, Y.; Zhou, H.; Sun, C.-J.; Sheehan, C.; Zhang, Z.; Wan, G.; Liu, Y.-S.; Guo, J.; Li, S.; Shin, H.; Hwang, S.; Gunnoe, T. B.; Goddard, W. A.; Zhang, S. Oxygen Evolution Reaction over Catalytic Single-Site CO in a Well-Defined Brookite TiO_2 Nanorod Surface. *Nat. Catal.* **2021**, *4*, 36−45.
(51) Hossain, M. D.; Huang, Y.; Yu, T. H.; Goddard, W. A., III; Luo, Z. Reaction Mechanism and Kinetics for CO_2 Reduction on Nickel Single Atom Catalysts from Quantum Mechanics. *Nat. Commun.* **2020**, *11*, 2256.
(52) Garza, A. J.; Bell, A. T.; Head-Gordon, M. Mechanism of CO_2 Reduction at Copper Surfaces: Pathways to C2 Products. *ACS Catal.* **2018**, *8*, 1490−1499.
(53) Nie, X.; Esopi, M. R.; Janik, M. J.; Asthagiri, A. Selectivity of CO_2 Reduction on Copper Electrodes: The Role of the Kinetics of Elementary Steps. *Angew. Chem.* **2013**, *125*, 2519−2522.
(54) Raciti, D.; Wang, C. Recent Advances in CO_2 Reduction Electrocatalysis on Copper. *ACS Energy Lett.* **2018**, *3*, 1545−1556.
(55) Nitopi, S.; Bertheussen, E.; Scott, S. B.; Liu, X.; Engstfeld, A. K.; Horch, S.; Seger, B.; Stephens, I. E. L.; Chan, K.; Hahn, C.; Nørskov, J. K.; Jaramillo, T. F.; Chorkendorff, I. Progress and Perspectives of Electrochemical CO_2 Reduction on Copper in Aqueous Electrolyte. *Chem. Rev.* **2019**, *119*, 7610−7672.
(56) Zhi, X.; Jiao, Y.; Zheng, Y.; Vasileff, A.; Qiao, S.-Z. Selectivity Roadmap for Electrochemical CO_2 Reduction on Copper-Based Alloy Catalysts. *Nano Energy* **2020**, *71*, 104601.

https://doi.org/10.1021/acs.jpcc.1c07484
J. Phys. Chem. C 2021, 125, 23773−23783